three-dimensional (3D) crystals[22], containing H^+-ATPase (1 mg ml^{-1}), dodecylmaltoside (1.28 mg ml^{-1}), threhalose (0.1%), ammonium sulphate (100 mM) and PEG4000 (Fluka) (10.5% w/v) in 30G solution[18], on carbon-coated electron-microscope grids. Details of the crystallization procedure will be given elsewhere.

Grids were blotted for 5 to 10 s, frozen in liquid ethane[23], transferred at liquid-nitrogen temperature into a Gatan cryotransfer specimen holder and observed at ~100 K in a Philips CM200 FEG electron microscope operated at 200 kV acceleration voltage. Other grids were mounted in a modified Leica KF80 rapid-freezing apparatus for transfer into a JEOL 3000SFF electron microscope operated at 300 kV, equipped with a top-entry cryo-stage cooled to 4 K with liquid helium. Images were taken with 1 or 2 s exposure time. Most images recorded with the Philips CM200FEG were taken using a spot-scan procedure (I. Tews and W.K., unpublished) at a total dose of ~10 eÅ^{-2}. Images at tilt angles above 45° were recorded with the JEOL 3000 SFF at a total dose of ~25 eÅ^{-2} in flood-beam mode. At these high tilt angles, the increased mean free path of 300 kV electrons was an advantage, as the effective specimen thickness at 60° tilt is ~500 Å. Images were recorded under low-dose conditions at a magnification of 50,000 on Kodak SO-163 film and developed for 12 min with full-strength Kodak D19.

Micrographs were screened by optical diffraction. 60 out of ~600 images were selected. Areas of 8,000 × 8,000 pixels were digitized using a Zeiss SCAI scanner with a 7-μm step size. Images were processed on a DEC/Alpha workstation using MRC image-processing programs[24]. Phase comparison of symmetry-related reflections from untilted images indicated $P321$ symmetry. Only crystals with actual tilt angles of less than 5° showed the projection symmetry clearly, owing to their unusual thickness of ~240 Å. After three cycles of unbending and correction for the contrast transfer function, amplitude and phase data of 60 images of tilt ranges 0° to 60° (Table 1) were merged. Two rounds of refinement of the tilt angle and tilt axis angle of the individual images against the merged data set resulted in an improvement of the average phase residual from 35 to 26°. Lattice lines (Fig. 1) were plotted with merged amplitudes and phases and manually truncated at points where the scatter of the observed phases approached random. The point-spread function indicated a nominal maximum resolution of 8 Å in the x–y plane and 22 Å in the perpendicular direction. A three-dimensional density map was calculated with the CCP4 program suite[25] with or without applying a negative temperature factor. The map was displayed with the graphics programs O (ref. 26) or AVS[27]. Adjacent monomers related by non-crystallographic 6-fold symmetry were masked and averaged using the program SPIDER[28].

1. Scarborough, G. A. in *Handbook of Biological Physics* Vol. 2 (eds Konings, W. N., Kaback, H. R. & Lolkema, J. S.) 75–92 (Elsevier Science, Amsterdam, 1996).
2. Scarborough, G. A. in *Molecular Aspects of Transport Proteins* (ed. de Pont, J. J. H. H. M.) 117–134 (Elsevier, Amsterdam, 1992).
3. Nakamoto, R. K. & Slayman, C. W. Molecular properties of the fungal plasma-membrane H^+-ATPase. *J. Bioenerg. Biomemb.* **21,** 621–632 (1989).
4. Nakamoto, R. K., Rao, R. & Slayman, C. W. Transmembrane segments of the P-type cation-transporting ATPases. *Ann. N. Y. Acad. Sci.* **574,** 165–179 (1989).
5. Mandala, S. M. & Slayman, C. W. The amino and carboxyl termini of the *Neurospora* plasma membrane H^+-ATPase are cytoplasmically located. *J. Biol. Chem.* **264,** 16276–16281 (1989).
6. Hennessey, J. P. Jr & Scarborough, G. A. Direct evidence for the cytoplasmic location of the NH_2- and COOH-terminal ends of the *Neurospora crassa* plasma membrane H^+-ATPase. *J. Biol. Chem.* **265,** 532–537 (1990).
7. Scarborough, G. A. & Hennessey, J. P. Jr Identificaton of the major cytoplasmic regions of the *Neurospora crassa* plasma membrane H^+-ATPase using protein chemical techniques. *J. Biol. Chem.* **265,** 16145–16149 (1990).
8. Rao, U. S., Hennessey, J. P. Jr & Scarborough, G. A. Identification of the membrane-embedded regions of the *Neurospora crassa* plasma membrane H^+-ATPase. *J. Biol. Chem.* **266,** 14740–14746 (1991).
9. Rao, U. S., Bauzon, D. D. & Scarborough, G. A. Cytoplasmic location of amino acids 359–440 of the *Neurospora crassa* plasma membrane H^+-ATPase. *Biochim. Biophys. Acta* **1108,** 153–158 (1992).
10. Goormaghtigh, E., Chadwick, C. & Scarborough, G. A. Monomers of the *Neurospora* plasma membrane H^+-ATPase catalyse efficient proton translocation. *J. Biol. Chem.* **261,** 7466–7471 (1986).
11. Chadwick, C., Goormaghtigh, E. & Scarborough, G. A. A hexameric form of the *Neurospora crassa* plasma membrane H^+-ATPase. *Arch. Biochem. Biophys.* **252,** 348–356 (1987).
12. Henderson, R. & Unwin, P. N. T. Three-dimensional model of purple membrane obtained by electron microscopy. *Nature* **257,** 28–32 (1975).
13. Henderson, R. *et al.* Model for the structure of bacteriorhodopsin based on high-resolution electron cryo-microscopy. *J. Mol. Biol.* **213,** 899–929 (1990).
14. Kühlbrandt, W., Wang, D. N. & Fujiyoshi, Y. Atomic model of plant light-harvesting complex by electron crystallography. *Nature* **367,** 614–621 (1994).
15. Walz, T. *et al.* The three-dimensional structure of aquaporin-1. *Nature* **387,** 624–627 (1997).
16. Cheng, A., v. Hoek, A. N., Yeager, M., Verkman, A. S. & Mitra, A. Three-dimensional organisation of a human water channel. *Nature* **387,** 627–630 (1997).
17. Li, H., Lee, S. & Jap, B. Molecular design of aquaporin-1 water channel as revealed by electron crystallography. *Nature Struct. Biol.* **4,** 263–265 (1997).
18. Cyrklaff, M., Auer, M., Kühlbrandt, W. & Scarborough, G. A. 2-D structure of the *Neurospora crassa* plasma membrane ATPase as determined by electron cryomicroscopy. *EMBO J.* **14,** 1854–1857 (1995).
19. Goormaghtigh, E., Vigneron, L., Scarborough, G. A. & Ruysschaert, J.-M. Tertiary conformational changes of the *Neurospora crassa* plasma membrane H^+-ATPase monitored by hydrogen/deuterium exchange kinetics: a Fourier transform infrared spectroscopy approach. *J. Biol. Chem.* **269,** 27409–27413 (1994).
20. Toyoshima, C., Sasabe, H. & Stokes, D. L. Three-dimensional cryo-electron microscopy of the calcium ion pump in the sarcoplasmic reticulum membrane. *Nature* **362,** 469–471 (1993).
21. Serrano, R. Structure and function of proton translocating ATPase in plasma membranes of plants and fungi. *Biochem. Biophys. Acta* **947,** 1–28 (1988).
22. Scarborough, G. A. Large single crystals of the *Neurospora crassa* plasma membrane H^+-ATPase: An approach ot the crystallisation of integral membrane proteins. *Acta Crystallogr. D* **50,** 643–649 (1994).
23. Dubochet, J. *et al.* Cryo-electron microscopy of vitrified specimens. *Quart. Rev. Biophys.* **21,** 129–228 (1988).
24. Crowther, R. A., Henderson, R. & Smith, J. M. MRC image processing programs. *J. Struct. Biol.* **116,** 9–16 (1996).
25. Collaborate Computational Project No. 4. The CCP4 suite: Programs for protein crystallography. *Acta Crystallogr. D* **50,** 760–763 (1994).
26. Jones, T. A., Zou, J. Y., Cowan, S. W. & Kjeldgaard, M. Improved methdos for building protein models in electron density maps. *Acta Crystallogr. A* **47,** 110–119 (1991).
27. Sheehan, B., Fuller, S. D., Piqus, M. E. & Yeager, M. AVS software for visualisation in molecular biology. *J. Struct. Biol.* **116,** 99–106 (1996).
28. Frank, J. *et al.* SPIDER and WEB: Processing and visualisation of images in 3D electron microscopy and related fields. *J. Struct. Biol.* **116,** 190–199 (1996).
29. Kühlbrandt, W. Discrimination of protein and nucleic acids by electron microscoy using contrast variation. *Ultramicroscopy* **7,** 221–232 (1982).
30. Unwin, P. N. T. & Ennis, P. D. Two configurations of a channel-forming membrane protein. *Nature* **307,** 609–613 (1984).

corrections

The effect of sedimentary cover on the flexural strength of continental lithosphere

Luc L. Lavier & Michael S. Steckler

Nature **389,** 476–479 (1997)
....
The last term on the right-hand side of equation (1) should read

$$\left(\frac{\dot{\varepsilon}}{A}\right)^{1/n} \int_{z_2}^{z_3} e^{u(z)} dz$$

to make it consistent with an integration over the variable z rather than over the function $u(z)$. □

Requirement for IRF-1 in the microenvironment supporting development of natural killer cells

Kouetsu Ogasawara, Shigeaki Hida, Nazli Azimi, Yutaka Tagaya, Takeo Sato, Taeko Yokochi-Fukuda, Thomas A. Waldmann, Tadatsugu Taniguchi & Shinsuke Taki

Nature **391,** 700–703 (1998)
....
In the second sentence of the second paragraph on page 701, interleukin-5 should be interleukin-15. □

14. Matthews, R. K. Tectonic implications of glacio-eustatic sea-level fluctuations. *Earth Planet. Sci. Lett.* **5**, 459–462 (1969).
15. Wallmann, P. C., Mahood, G. A. & Pollard, D. D. Mechanical models for correlation of ring-fracture eruptions at Pantelleria, Strait of Sicily, with glacial sea-level drawdown. *Bull. Volcanol.* **50**, 327–339 (1988).
16. Zielinski, G. A. *et al.* Volcanic aerosol records and tephrochronology of the Summit, Greenland, ice cores. *J. Geophys. Res.* (in the press).
17. Paterne, M., Labeyrie, J., Guichard, F., Mazaud, A. & Maitre, F. Fluctuations of the Campanian explosive volcanic activity (south Italy) during the past 190,000 years, as determined by marine tephrochronology. *Earth. Planet Sci. Lett.* **98**, 166–174 (1990).
18. Paterne, M. & Guichard, F. Triggering of volcanic pulses in the Campanian area, south Italy, by periodic deep magma influx. *J. Geophys. Res.* **98**, 1861–1873 (1993).
19. Blanchon, P. & Shaw, J. Reef drowning during the last glaciation: evidence for catastrophic sea-level rise and ice-sheet collapse. *Geology* **23**, 4–8 (1995).
20. Cox, D. R. & Lewis, P. A. W. *The Statistical Analysis of Series of Events* 2nd edn (Methuen, London, 1978).
21. Solow, A. R. Testing for change in the frequency of El Niño events. *J. Clim.* **8**, 2563–2566 (1995).
22. Bebbington, M. S. & Lal, C. D. On homogeneous models for volcanic eruptions. *Math. Geol.* **28**, 585–600 (1996).
23. Fairbanks, R. .C. A 17,000-year glacio-eustatic sea-level record: influence of glacial melting rates on the Younger Dryas event and deep-ocean circulation. *Nature* **342**, 637–642 (1989).
24. Shackleton, N. J. Oxygen isotopes, ice volume and sea level. *Quat. Sci. Rev.* **6**, 183–190 (1987).
25. Cleveland, W. S., Grosse, E. & Shyu, W. M. in *Statistical Models in S* (eds Chambers, J. M. & Hastie, T.) 309–376 (Wadsworth & Brooks/Cole, Pacific Grove, CA, 1992).

The effect of sedimentary cover on the flexural strength of continental lithosphere

Luc L. Lavier[*†] **& Michael S. Steckler**[*]

* Lamont-Doherty Earth Observatory, † Department of Earth and Environmental Sciences, Columbia University, PO Box 1000, RT 9W, Palisades, New York 10964–8000, USA

The factors that control the flexural rigidity—or effective elastic thickness (EET)—of continental lithosphere have been extensively studied over the past two decades. Using EET estimates derived from the analysis of topography, basin structures and gravity anomalies, several authors[1–5] have shown that crustal thickness, geothermal gradient, strain rate, rheology and plate curvature all affect the flexural strength of continents. Recognition that certain combinations of these parameters result in a significant reduction of flexural strength caused by decoupling of the crust and the upper mantle[3,5] has been a critical step in understanding why many continental areas have estimated EETs that are thin compared with the total mechanical thickness of the continental lithosphere[5]. Here we develop a semi-analytical model of the EET through a parametrization of the yield stress envelope[6,7] that includes the effects of crust–mantle decoupling. We perform a detailed comparison of EET estimates at foreland basins and mountain belts to values predicted by our model and find that, to predict the EET estimates successfully, we need to take into account the effect of the sediment cover and to use a strong plagioclase-controlled rheology. The effect of sediment cover is to weaken the lithosphere because of the lower density of sediments relative to crystalline crust[5,8,9] and by thermally insulating the lower crust[9–11].

The yield stress envelope (YSE)[6] is one of the keys to understanding the variations of strength in the oceanic and continental lithosphere[5,7,11]. It allows the parametrization of EET because it defines bounds on the elastic stresses that the lithosphere can sustain (Fig. 1). We formulate a model of flexural strength by assuming a double-layered brittle–elastic–plastic YSE for the continental lithosphere. In the brittle parts of the lithosphere, the yield stress follows Byerlee's law[12] (Fig. 1). By thin plate theory, the bending stress

within the elastic portion of the plate is linearly dependent on plate curvature (Fig. 1). The yield stress in the ductile lower crust and lower lithospheric mantle follows power-law dislocation creep[12,13] represented by quasi-exponential curves (Fig. 1).

We derive semi-analytic expressions for the in-plane stress, T, and bending moment, M, for the flexing lithosphere by approximating the geotherm as a linear function of depth where the strength is controlled by ductile flow. The stress distribution, $\sigma(z)$, depends explicitly on the crustal thickness, the rheology of the continental lithosphere, the geotherm and the sediment thickness. Integrating, for a single layer we obtain:

$$T = \int \sigma(z)\,dz = \gamma\tfrac{1}{2}(z_1 - z')^2 + \ddot{w}_0[\tfrac{1}{2}(z_2^2 - z_1^2) - z_0(z_2 - z_1)]$$
$$+ \left(\frac{\dot{\epsilon}}{A}\right)^{2/n} \frac{Q_A}{nRc} \int_{z_2}^{z_3} e^{u(z)}\,dz \qquad (1)$$

where z_0 is the depth of the neutral surface; z_1 and z_2 represent the depth of the brittle–elastic boundary and the elastic–ductile boundary, respectively; and z_3 is the depth to the base of the YSE (Fig. 1). We have $z' = \{[\rho_c - \rho_s(z_s)]/\rho_c\}z_s$, where z_s is the depth of the bottom of the sediment layer and ρ_s and ρ_c are the average sediment and crustal densities, respectively. We have $\gamma = 0.67\bar{\rho}g$ or $\gamma = -2.21\bar{\rho}g$ for tension and compression, respectively, and $\ddot{w}_0 = E/(1 - v^2)\ddot{w}$, where $\ddot{w}$ is the curvature of the lithosphere, E is Young's modulus and v is Poisson's ratio. A is the power law pre-exponent, n the power law exponent and Q_A the activation energy. Finally, $u(z) = Q_A/[nR(T_0 + cz)]$, with T_0 and c as the zero intercept temperature and geothermal gradient for the best-fitting linear geotherm; R is the universal gas constant.

Equation (1) neglects some minor additional strength due to the variation of sediment density with depth. Similarly to the formulation in Bodine *et al.*[7], the stress distribution, in-plane stress and bending moment are functions of the depths z_1 and z_2. By specifying the curvature and in-plane stress, we solve equation (1) numerically to obtain z_1 and z_2. Then we determine the stress distribution and calculate the bending moment, M:

$$M = \int \sigma(z)\,z\,dz \qquad (2)$$

The flexural rigidity, D, can be calculated for any given value of the lithospheric curvature by using $M = -D\ddot{w}$. Decoupling occurs
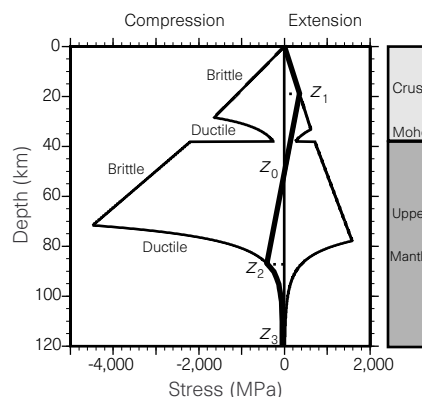

Figure 1 YSE of the continental lithosphere defining the maximum stress for which the lithosphere behaves like an elastic solid. The failure envelope of the crust and upper mantle forms a double layer, each consisting of a brittle upper part and ductile lower part. The heavy line shows an example of a bending stress profile. The lithosphere exhibits brittle failure from the surface to depth z_1, linear elastic behaviour from z_1 to z_2 and ductile failure below depth z_2; z_0 corresponds to the depth of no elastic strain.

when bending stresses in the lower crust become larger than the yield stresses. Equation (1) is then modified and solved for a double YSE. The effective elastic thickness of the lithosphere is calculated with:

$$D = [E/12(1 - v^2)]EET^3 \qquad (3)$$

For the modelling we use geotherms based on a 200 km equilibrium thickness for the lithosphere[14]. We calculate the geotherm for a given age of the lithosphere at the time of loading and a sediment thickness. We solve the heat equation by using a modified Fourier transform solution. The density and thermal conductivity of the sediments vary with depth according to compaction properties for a shaley sand[15], a lithology representative of most foreland basins. The initial porosity is 56%, the compaction depth constant is 2,564 m and the thermal conductivity is 3.8 W m^{-1} K^{-1}. Radiogenic heat generation is neglected for the sediments but is included for the crust. These values yield a conservative estimate of the effect of including the sediment cover. Loading by the sediment cover weakens the lithosphere in several ways: the low density of the sediments decreases the lithostatic pressure[9]; the low thermal conductivity of the sediment cover increases the temperature and decreases the yield stresses in the lower crust[9]; and the sedimentary layers increase the Moho depth, raising the lower crustal temperature.

In Fig. 2a we model the variation in EET caused by a change in crustal thickness for a continental lithosphere 1,000 Myr old at the time of loading. In agreement with Burov and Diament[5], a lithosphere with thick crust decouples for a smaller load or bending moment than its thermal equivalent with a thinner crust.

Figure 2b shows the effect of the sediment fill on flexural strength. For an average lithospheric structure similar to that of the Zagros foreland basin (Saudi Arabia–Iraq; see Table 1 and Fig. 3 for values), 5 km of sediment fill causes decoupling for curvatures $\geq 2 \times 10^{-7}$ m^{-1}. At this curvature the EET is reduced by 22 km. Comparison of the YSEs (Fig. 2b) highlights the effect of the sediment fill. In the absence of sediment fill, yield stresses in the lower crust are greater than the bending stresses and the lithosphere does not decouple. With sediments, yield stresses in the lower crust are smaller than the bending stresses and the lithosphere decouples, decreasing the EET.

We perform a detailed comparison of observed EET values estimated from studies of thrust belts at active and extinct plate boundaries to values predicted by our model (Table 1). To investigate the importance of weakening by sediment fill, we also consider a model parametrization that does not include the effects of the sediment cover (Fig. 3). The observed EET represents an average fit of the gravity anomaly across an area where the strength is variable. The average values are likely to be biased towards the dominant parts of the gravity anomaly signal. The lithospheric curvatures, estimated by fitting a circle to the depth of the base of the foreland basin sediments, are also an average that is biased towards the deeper part of the basin. Because they represent similar averages we can compare the predicted values of EET with the observed values of EET.

Our model successfully predicts the flexural rigidity of all of the examples except one (Fig. 3). We can discern three pools of values that illustrate the relative importance of sediments as a factor in controlling the flexural strength at continents. Where the litho-
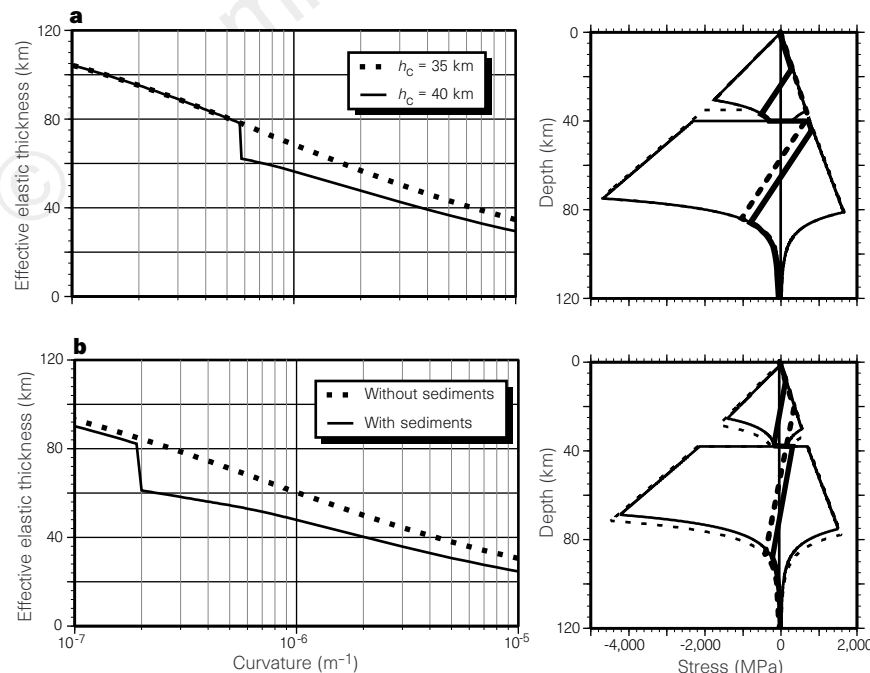

Figure 2 a, For 1,000-Myr-old lithosphere with a crust 35 km thick (dotted line), the EET decreases as curvature increases, but the lithosphere does not decouple. In the right panel, the corresponding YSE (broken light line) shows that the lower crust is always in the brittle field. Therefore, the lithosphere never decouples, as in the example bending stress profile with a curvature of 6 × 10^{-7} m^{-1}. For an equivalent lithosphere with a 40-km crust (solid lines) the Moho depth is greater and thus the lower crust is hotter. The YSE (light solid line) for the lower crust exhibits a ductile failure zone. For curvatures greater than 6 × 10^{-7} m^{-1}, the bending stresses (broken bold line) exceed the yield stress in the lower crust. This causes decoupling of the lithosphere. As a result, the bending stress profile readjusts (bold solid line) and the EET is reduced by ~20 km. **b**, Plot of the decrease in EET due to sediments. The 'with sediments' example (solid line) refers to a 600-Myr-old lithosphere with a 33-km crust and 5 km of sediments. 'Without sediments' (dotted line) refers to a similar lithosphere without sediments but with a 38-km crust to have an identical Moho depth. In the right panel, the YSE with a sediment cover is weaker than without a sediment cover owing primarily to the heating effect of the sediments. For the case without sediment cover, the EET decreases smoothly as the curvature increases. With sediment cover, the bending stresses in the lower crust exceed the yield stress of the lower crustal material for curvatures greater than 2 × 10^{-7} m^{-1}; as shown by the stress profile (bold solid line). The lithosphere decouples and the EET value drops by >20 km.

sphere is young and hot, and the crust sufficiently thick (Apennines, Eastern Alps, Western Alps), the lithosphere decouples regardless of the effect of the sediments. The parameters controlling the flexural strength are the age and the Moho depth. Where the lithosphere is old (>1,000 Myr) and cold (Ganges and Himalayas) and none of the weakening effects due to crustal thickness, curvature or sediment fill are sufficiently large, the lithosphere does not decouple. The flexural strength is controlled by the thickness and the rheology of the upper mantle. Finally, for the Tarim, Kunlun, Zagros, Southern Alps and Andes the age, the crustal thickness and the curvature alone are not enough to explain the observed EET values. There, the sediment fill plays a determining role by weakening an otherwise strong lithosphere. In these cases, the sediments cause a decrease of 8–30 km in the EET. The correct EET cannot be estimated without including the effect of the sediments.

Uncertainties on our modelling are described in Fig. 3. One source of uncertainty is critical to our modelling: the choice of rheological parameters for the lower crust[12,13].

For the lower crust we tested a set of weak rheologies (wet/dry quartzite and granite) and a set of stronger rheologies (diabase, anorthosite and quartz–diorite)[13]. The results show that when the creep is controlled by quartz rheology, the lithosphere is permanently decoupled[5] even in very old lithosphere (Ganges and Himalayas). But plagioclase-controlled creep rheologies are sufficiently strong to maintain coupling at the Ganges and the Himalayas, as required by their high EET values. Quartz–diorite is the weakest possible rheology that allows such a behaviour. For stronger crustal rheologies, sediments are required to induce decoupling at other basins. Here we show the model with dislocation creep rheologies corresponding to anorthosite for the lower crust and olivine for the upper mantle. The constants, taken from Kirby and Kronenberg[13], for anorthosite are $\log_{10}A = -3.5\,\mathrm{MPa^{-n}\,s^{-1}}$, $n = 3.2$, $Q_A = 238\,\mathrm{kJ\,mol^{-1}}$, and for olivine are $\log_{10}A = 4.46\,\mathrm{MPa^{-n}\,s^{-1}}$, $n = 3.6$, $Q_A = 535\,\mathrm{kJ\,mol^{-1}}$.
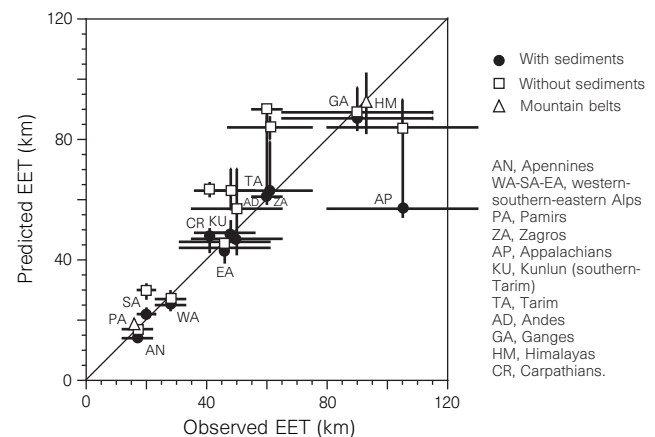
The Appalachian foreland is the one case in which we fail to predict the published EET of ~105 km (ref. 1). Several studies have

Table 1 Observations of EET and values used to calculate predicted EET

	D (10^{-23} N m)	Observed EET (km)	h_c (km)	$-\ddot{w}$ (10^{-7} m^{-1})	h_s (km)	Age (Myr)	Predicted EET (km)
Mountain belts							
Himalayas	~50	93 ± 15	60 ± 5	~3	–	1,000 ± 200	90^{+10}_{-10}
Pamir	~0.1	16 ± 4	70 ± 5	~50	–	300 ± 100	18^{+2}_{-2}
Foreland basins							
Western Alps	1–3	28 ± 5	30 ± 3	40 ± 10	3–5	250 ± 50	25^{+2}_{-5}
Eastern Alps	4.6–6	46 ± 7	30 ± 3	10 ± 10	2–4	350 ± 100	44^{+2}_{-2}
Southern Alps	0.24–1.9	20 ± 3	25 ± 3	50 ± 10	5–7	250 ± 50	22^{+2}_{-1}
Apennines	~0.24	~17	24 ± 3	40 ± 10	3–5	100 ± 50	14^{+2}_{-1}
Carpathians	2–4	40.5 ± 5	32 ± 3	10 ± 10	5–7	1,600 ± 200	49^{+2}_{-7}
Zagros	~10	~60	33 ± 3	2.5 ± 1	5–6	600 ± 200	61^{+27}_{-3}
Tarim	8.8–10	61 ± 14	35 ± 3	4 ± 1	5–7	800 ± 200	63^{+16}_{-2}
Kunlun	~5	~48	35 ± 3	15 ± 10	5–7	800 ± 200	49^{+4}_{-2}
Ganges	10–80	90 ± 25	35 ± 3	3 ± 1	3–5	1,000 ± 200	87^{+8}_{-4}
Appalachians	10–100	105 ± 25	37 ± 3	2 ± 1	2–4	600 ± 200	60^{+25}_{-2}
Andes	2–11	50 ± 15	35 ± 3	20 ± 20	3–5	1,000 ± 200	47^{+12}_{-5}

In this study we used observed EET values in areas for which we could obtain the input parameters (crustal thickness h_c, average curvature $\ddot{w}$, sediment thickness h_s, and thermal age at the time of loading) required for the model. The flexural rigidities were taken from ref. 5 and references therein and from refs 19–22. All values of observed EET were recalculated from the flexural rigidity, D, using $E = 5 \times 10^{10}$ N m^{-2} and $v = 0.3$. The standard deviation of observed EET values were used to estimate uncertainties. We used only observed flexural rigidities derived from forward modelling of gravity anomalies because spectral method estimates remain controversial[23]. The crustal thickness includes the thickness of sediments deposited before loading. The sediment thickness corresponds to the sediments deposited since the beginning of loading. The average curvature is derived from the horizon defining the base of h_s calculated on a spherical Earth. The age is the thermal age of the lithosphere at the time of loading. The uncertainties in h_c, h_s and $\ddot{w}$ correspond to uncertainties inherent in their measurement and to the variability observed in the cross-section from which the observed EET values were estimated. Large uncertainties in the average curvature are estimated owing to the limited data. We estimate the thermal age of the lithosphere as the difference between the age of the last major thermal event and the age of the beginning of collision. We assume uncertainties in the thermal age of 20–50% of the age determined from the literature. The references for crustal thickness, sediment thickness, the curvature and flexural rigidity are as follows: Zagros foredeep[24,25], Kunlun (South Tarim) foredeep[26,27], Ganges basin[1,4,28], Tarim foredeep[26,27], Andes foredeep[29,30], Appalachian foredeep[31,32], Carpathian foredeep[22,23,33,34], Apennine foredeep[35,36], Southern Alps[4,37,38], Eastern and Western Alps[4,37,38] and Himalayas and Pamirs[4,5,28,39].

Figure 3 Plot of the predicted values of EET against observed values of EET. Perfect agreement is represented by the diagonal line. For the predicted values we used different values of strain rate. For active convergent areas (Himalayas, Ganges basin, Pamirs, Kunlun, Andes and Tarim) we used $\dot{\epsilon} = 10^{-15}\,\mathrm{s^{-1}}$. For fossil convergent margins (Alps, Appalachians, Apennines, Zagros and Carpathians) we used $\dot{\epsilon} = 10^{-17}\,\mathrm{s^{-1}}$. The white squares represent the predicted fit without taking into account the sediments deposited since the beginning of loading. The filled dots represent the predicted fit taking account of the effect of the sediments. The open triangles represent the predicted fit for the mountain belts (Pamirs and Himalayas). Error bars on the predicted values of EET are calculated as the means of the uncertainties due to uncertainties in the determination of h_s, h_c, $\ddot{w}$, the thermal age and the strain rate. Uncertainties in the predicted EET values due to uncertainties in the thermal age determinations vary between 2% and 10% for the areas with thermal ages greater than 600 Myr, and between 10% and 28% for areas with thermal ages from 100 to 350 Myr, the uncertainty being largest for the youngest age. The lithosphere is stronger at high strain rates than at low strain rates[5] owing to the non-newtonian behaviour of power-law creep. An order of magnitude change in strain rate produces a change of 10–15% in the EET value. When the effect of the sediment cover is not included, an increase in curvature can cause decoupling for only two cases, TA and AP, as shown by the error bars for the predicted values. Overall, the model successfully predicts the EET values for most locations. The only observed value that is not fitted is the value for the Appalachian foredeep as discussed in the text.

● With sediments
□ Without sediments
△ Mountain belts

AN, Apennines
WA-SA-EA, western-southern-eastern Alps
PA, Pamirs
ZA, Zagros
AP, Appalachians
KU, Kunlun (southern-Tarim)
TA, Tarim
AD, Andes
GA, Ganges
HM, Himalayas
CR, Carpathians.

not corroborated this high value[16–18]. Quinlan and Beaumont[16] matched the stratigraphy of the Appalachian basin by using a layered visco-elastic model that had an average EET of 67 km. Although they note that a pure elastic plate model does not adequately reproduce the stratigraphy, elastic plate models in which the EET decreases with curvature would produce offlapping stratigraphic patterns as seen in the observed stratigraphy. Recently, Stewart and Watts[17] re-estimated the EET of several mountain belts by using a variable-rigidity formulation. Converting their estimates to the values of E and v used in this paper gives a range of 50–88 km for the EET. These studies suggest that the high value found by Karner and Watts[1] is an overestimate and that a lower value averaging ~65–70 km is a better estimate. If so, our prediction of 60 km is within uncertainties.

We have established a parametrization of flexural strength at continents based on the yield stress envelope that successfully predicts the EET of the continental lithosphere at foreland basins and mountain belts. We have also demonstrated the importance of sediment fill as parameter controlling flexural strength at continents. The sediment cover is most likely to control the value of EET in places where the lithosphere's crust is thin compared with an average 35-km-thick continental crust[5], the age of the lithosphere is close to its thermal equilibrium and for which the sediment cover reaches thicknesses greater than 3–5 km. Accounting for the effect of sediments and crustal thickness should facilitate the evaluation of the flexural strength at other types of basins and continental margins. □

1. Karner, G. D. & Watts, A. B. Gravity anomalies and flexure of the lithosphere at mountain ranges. *J. Geophys. Res.* **88**, 10449–10477 (1983).
2. Kusznir, N. & Karner, G. D. Dependence of the flexural rigidity of the continental lithosphere on rheology and temperature. *Nature* **316**, 138–142 (1985).
3. McNutt, M. K., Diament, M. & Kogan, M. G. Variations of elastic plate thickness at continental thrust belts. *J. Geophys. Res.* **93**, 8825–8838 (1988).
4. Royden, L. H. The tectonic expression slab pull at continental convergent boundaries. *Tectonics* **12**, 303–325 (1993).
5. Burov, E. G. & Diament, M. The effective elastic thickness of the continental lithosphere: what does it really mean? *J. Geophys. Res.* **100**, 3905–3927 (1995).
6. Goetze, C. & Evans, B. Stress and temperature in the bending lithosphere as constrained by experimental rock mechanics. *Geophys. J. R. Astron. Soc.* **59**, 463–478 (1979).
7. Bodine, J. H., Steckler, M. S. & Watts, A. B. Observations of flexure and the rheology of the oceanic lithosphere. *J. Geophys. Res.* **86**, 3695–3707 (1981).
8. Cloetingh S., Wortel, M. J. R. & Vlaar, N. J. Evolution of passive continental margins and initiation of subduction zones. *Nature* **297**, 139–142 (1982).
9. Steckler, M. S. & ten Brink, U. S. Lithospheric strength variations as a control on new plate boundaries: examples from the northern Red Sea region. *Earth Planet. Sci. Lett.* **79**, 120–132 (1986).
10. Karner, G. D. Sediment blanketing and the flexural strength of extended continental lithosphere. *Basin Res.* **3**, 177–185 (1991).
11. Molnar, P. & Tapponnier, P. A possible dependence of tectonic strength on the age of the crust in Asia. *Earth Planet. Sci. Lett.* **52**, 107–114 (1981).
12. Kohlstedt, D. L., Evans, B. & Mackwell, S. J. Strength of the lithosphere: constraints imposed by laboratory experiments. *J. Geophys. Res.* **100**, 17587–17602 (1995).
13. Kirby, S. H. & Kronenberg, A. K. Rheology of the lithosphere. *Rev. Geophys.* **25**, 1219–1244 (1987).
14. Zhang, Y.-S. & Tanimoto, T. High-resolution global upper mantle structure and plate tectonics. *J. Geophys. Res.* **98**, 9793–9823 (1993).
15. Sclater, J. G. & Christie, P. A. F. Continental stretching; an explanation of the post-Mid-Cretaceous subsidence of the central North Sea basin. *J. Geophys. Res.* **85**, 3711–3739 (1980).
16. Quinlan, G. M. & Beaumont, C. Appalachian thrusting, lithospheric flexure, and the Paleozoic stratigraphy of the Eastern interior of North America. *Can. J. Earth Sci.* **21**, 973–996 (1984).
17. Stewart, J. & Watts, A. B. Gravity anomalies and spatial variations of flexural rigidity at mountain ranges. *J. Geophys. Res.* **102**, 5327–5353 (1997).
18. Turcotte, D. L. & Shubert, G. *Geodynamics. Applications of Continuum Physics to Geological Problems*, 131–133 (Wiley, New York, 1982).
19. Snyder, D. B. & Barazangi, M. Deep crustal structure and flexure of the Arabian plate beneath the Zagros collisional mountain belt as inferred from gravity observations. *Tectonics* **5**, 361–373 (1986).
20. Watts, A. B., Lamb, S. H., Fairhead, J. D. & Dewey, J. F. Lithospheric flexure and bending of the central Andes. *Earth Planet. Sci. Lett.* **134**, 9–21 (1995).
21. Royden, L. H. & Karner, G. D. Flexure of lithosphere beneath Apennine and Carpathian foredeep basins: evidence for an insufficient topographic load. *Am. Ass. Petrol. Geol. Bull.* **68**, 704–712 (1984).
22. Macario, A., Malinverno, A. & Haxby, W. F. On the robustness of elastic thickness estimates obtained using the coherence method. *J. Geophys. Res.* **100**, 15163–15172 (1995).
23. Royden, L. H. & Burchfiel, B. C. Are systematic variations in thrust belt style related to plate boundary processes? (The western Alps versus the Carpathians). *Tectonics* **8**, 51–61 (1989).
24. Seber, D., Valve, M., Sandvol, E., Steer, D. & Barazangi, M. Middle East Tectonics: applications of Geographic Information Systems (GIS). *GSA Today* **7**(2), 1–6 (1997).
25. Koop, W. J. & Stoneley, R. Subsidence history of the Middle East Zagros Basin, Permian to Recent. *Phil. Trans. R. Soc. Lond.* A **305**, 149–168 (1982).
26. Fan, P. & Ma, B. L. *Generan Petroleum Geology of the Tarim Basin*, Vol. 1, 1–21 (Academia Sinica, Science Press, Beijing, 1990).
27. Teng, J. W. *Geophysical Fields and Hydrocarbon Prospects of the Tarim Basin*, Vol. 2, 24–40 (Academia Sinica, Science Press, Beijing, 1991).
28. Verma, R. K. Gravity field and nature of continent–continent collision along the Himalaya. *Phys. Chem. Earth* **18**, 385–403 (1991).
29. Wigger, J. W. *et al.* in *Tectonics of the Southern Central Andes, Structure and Evolution of an Active Continental Margin* (eds Reutter, K.-J., Scheuber, E. & Wigger, P. J.) 23–48 (Springer, Berlin, 1994).
30. Dunn, J. F., Hartshorn, K. G. & Hartshorn, P. W. in *Petroleum Basins of South America* (eds Tankard, A. J., Suárez Soruco, R. & Welsink, H. J.) 523–543 (Am. Ass. Petrol. Geol. Mem. 62, 1995).
31. Hinze, W. J. & Braile, L. W. in *The Geology of North America*, Vol. D-2 (*Sedimentary Cover–North American Craton: U.S.*) (Geological Society of America, Boulder, CO, 1988).
32. Rankin, D. W. *et al.* in *Centenial Continent/Ocean Transect* Vol. E-4 *Central Kentucky to Carolina Trough* 2 sheets (Geological Society of America, Boulder, CO, 1991).
33. Roure, F., Roca, E. & Sassi, W. The Neogene evolution of the outer Carpathian flysch units (Poland, Ukraine and Romania): kinematics of a foreland/fold-and-thrust belt system. *Sediment. Geol.* **86**, 177–201 (1993).
34. Raileanu, V., Talos, D., Varodin, V. & Stiopol, D. Crustal seismic reflection profiling in Romania on the Urziceni–Mizil line. *Tectonophysics* **223**, 401–409 (1993).
35. Buness, H. in *Joint Interpretation of Geophysical and Geological Data Applied to Lithospheric Studies* (eds Giese, P. *et al.*) 193–215 (Kluwer, Dordrecht, 1991).
36. Ori, G. G. Continental depositional systems of the Quaternary of the Po plain (northern Italy). *Sediment Geol.* **83**, 1–14 (1993).
37. Mueller, S. in *Mountain Building Processes* (ed. Hsue, K. J.) 181–199 (Academic, London, 1982).
38. Khale, H. G., Klingele, E., Mueller, S. & Egloff, R. The variation of crustal thickness across the Swiss Alps based on gravity and explosion seismic data. *Pure Appl. Geophys.* **114**, 479–494 (1976).
39. Beloussov, V. V. *et al.* Structure of the lithosphere along the Deep Seismic Sounding profile: Tien Shan–Pamirs–Karakorum–Himalaya. *Tectonophysics* **70**, 193–221 (1980).

Failure of plume theory to explain midplate volcanism in the southern Austral islands

M. K. McNutt*, **D. W. Caress**†, **J. Reynolds**‡, **K. A. Jordahl***§ **& R. A. Duncan**∥

* *Department of Earth, Atmospheric, and Planetary Sciences, Massachusetts Institute of Technology, Cambridge, Massachusetts 02139, USA*
† *SeaBeam Instruments, 141 Washington Street, East Walpole, Massachusetts 02032, USA, and Lamont-Doherty Earth Observatory, Palisades, New York 10964, USA*
‡ *Monterey Bay Aquarium Research Institute, PO Box 628, Moss Landing, California 95039, USA*
§ *MIT/Woods Hole Oceanographic Institute Joint Program in Oceanography and Applied Ocean Science and Engineering, Woods Hole, Massachusetts 02543, USA*
∥ *College of Oceanic and Atmospheric Sciences, Oregon State University, Corvallis, Oregon 97331, USA*

....

It has long been recognized that the properties of the Cook–Austral chain (Fig. 1) of volcanoes in the South Pacific are difficult to reconcile with the theory that volcanic activity in plate interiors is produced by the drift of tectonic plates over narrow, stationary plumes[1] of hot mantle material upwelling from depth. Radiometric dates[2,3] from many island samples are younger or older than would be predicted if a single plume currently located at volcanically active Macdonald seamount[4] was responsible for all of the volcanoes. Indeed, only the southernmost part of the Austral volcanic line has hitherto appeared to be consistent with plume activity, and then only within the past 6 million years (Myr)[5,6]. Here we report radiometric dates that demonstrate that these southern Austral volcanoes are actually composed of three distinct volcanic chains with a range of ages spanning 34 Myr and with inconsistent age progressions. Gravity anomalies and seafloor fabric suggest that the volume and location of volcanism in this region is controlled by stress in the lithosphere rather than the locus of narrow plumes rising from the deep Earth.

Our data were collected during a two-month expedition to the southeastern end of the Austral chain of volcanoes (Fig. 2) aboard the RV *Maurice Ewing* in March–May 1996. Our detailed mapping reveals that, in addition to the well-known Macdonald chain, there are two other lines of volcanoes, which we have named the

visual response as reflected in the VEP. Therefore, spectral analysis was performed using a recursive least-squares adaptive filter[24] to separate the VEP from the background EEG. The filter provided estimates of evoked response amplitude and phase over a 1 second running window. Six to nine individual 10-second trials were coherently averaged in the frequency domain to form averaged records of the Fourier amplitude of the second harmonic response (11 Hz) relative to the grating temporal frequency (5.5 Hz). Error statistics for averaged response amplitude were calculated using the T_{circ}^2 statistic[25], which also provided statistical significance values for discriminating stimulus-driven VEPs from background EFG.

We estimated contrast thresholds from the averaged records by extrapolating the response versus contrast function to $0\,\mu V$ using linear regression[14] (Fig. 2). The limits for the regression were selected using a combination of phase consistency and signal-to-noise ratio (SNR) criteria[8]. We calculated SNR on the basis of response amplitude and background EEG, the latter being estimated by averaging the EEG at two temporal frequencies, one just above and one just below the recording frequency. Background EEG amplitudes were not affected by visual stimulation: background levels remained constant throughout the 10-s sweep trials in both grating-alone and grating-plus-noise conditions, and the addition of external stimulus noise had no effect on background EEG levels (for example, for the youngest infants background EEG was 0.28 ± 0.046 microvolts in the grating-alone condition and 0.29 ± 0.042 microvolts in the condition with added high-contrast noise). Saturating portions of the contrast response function were excluded from the regression.

1. Atkinson, J., Braddick, O. & Braddick, F. Acuity and contrast sensitivity of infant vision. Nature 247, 403–404 (1974).
2. Harris, L., Atkinson, J. & Braddick, O. Visual contrast sensitivity of a 6-month-old infant measured by the evoked potential. Nature 264, 570–571 (1976).
3. Norcia, A. M., Tyler, C. W. & Hamer, R. D. High visual contrast sensitivity in the young human infant. Invest. Ophthalmol. Vis. Sci. 29, 44–49 (1988).
4. Norcia, A. M., Tyler, C. W. & Hamer, R. D. Development of contrast sensitivity in the human infant. Vision Res. 30, 1475–1486 (1990).
5. Pirchio, M., Spinelli, D., Fiorentini, A. & Maffei, L. Infant contrast sensitivity evaluated by evoked potentials. Brain Res. 141, 179–184 (1978).
6. Banks, M. S. & Bennett, P. J. Optical and photoreceptor immaturities limit spatial and chromatic vision of human neonates. J. Opt. Soc. Am. 5, 2059–2079 (1988).
7. Wilson, H. R. Development of spatiotemporal mechanisms in the human infant. Vision Res. 28, 611–628 (1988).
8. Norcia, A. M., Clarke, M. & Tyler, C. W. Digital filtering and robust regression techniques for estimating sensory thresholds from the evoked potential. IEEE Engng Med. Biol. 4, 26–32 (1985).
9. Norcia, A. M., Tyler, C. W., Hamer, R. D. & Wesemann, W. Measurement of spatial contrast sensitivity with the swept contrast VEP. Vision Res. 29, 627–637 (1989).
10. Tyler, C. W., Apkarian, P., Levi, D. M. & Nakayama, K. Rapid assessment of visual function: an electronic sweep technique for the pattern evoked potential. Invest. Ophthalmol Vis. Sci. 18, 703–713 (1979).
11. Pelli, D. G. in Vision: Coding and Efficiency (ed. Blackmore, C.) 1–24 (Cambridge University Press, Cambridge, 1990).
12. Bonds, A. B. Temporal dynamics of contrast gain in single cells of the cat striate cortex. Vis. Neurosci. 6, 239–255 (1991).
13. Morrone, M. C. & Burr, D. C. Evidence for the existence and development of visual inhibition in humans. Nature 321, 235–237 (1986).
14. Campbell, F. W. & Maffei, L. Electrophysiological evidence for the existence of orientation and size detectors in the human visual system. J. Physiol. (Lond.) 207, 635–652 (1970).
15. Yuodelis, C. & Hendrickson, A. A qualitative and quantitative analysis of the human fovea during development. Vision Res. 26, 847–855 (1986).
16. Shannon, E., Skoczenski, A. M. & Banks, M. S. Retinal illuminance and contrast sensitivity in human infants. Vision Res. 36, 67–76 (1996).
17. Van Nes, F. L. & Bouman, M. A. Spatial modulation transfer in the human eye. J. Opt. Soc. Am. 57, 401–406 (1967).
18. Geisler, W. S. & Albrecht, D. G. Cortical neurons: isolation of contrast gain control. Vision Res. 32, 1409–1410 (1992).
19. Ohzawa, I., Sclar, G. & Freeman, R. D. Contrast gain control in the cat's visual system. J. Neurophysiol. 54, 651–667 (1985).
20. Burr, D. C. & Morrone, M. C. Inhibitory interactions in the human vision system revealed in pattern-evoked potentials. J. Physiol. (Lond.) 389, 1–21 (1987).
21. Shapley, R. M. & Victor, J. D. The effect of contrast on the transfer properties of cat retinal ganglion cells. J. Physiol. (Lond.) 285, 275–298 (1978).
22. Skoczenski, A. M., O'Keefe, L. P., Kiorpes, L., Tang, C., Hawken, M. J. & Movshon, J. A. Visual efficiency of macaque LGN neurons. Neurosci. Abstr. 20, 7 (1994).
23. Pelli, D. G. & Zhang, L. Accurate control of contrast on microcomputer displays. Vision Res. 31, 1337–1350 (1991).
24. Tang, Y. & Norcia, A. M. An adaptive filter for the steady-state VEP. Electroencephalogr. Clin. Neurophysiol. 96, 268–277 (1994).
25. Victor, J. D. & Mast, J. A new statistic for steady-state evoked potentials. Electroencephalogr. Clin. Neurophysiol. 78, 378–388 (1991).

Requirement for IRF-1 in the microenvironment supporting development of natural killer cells

Kouetsu Ogasawara*, Shigeaki Hida*, Nazli Azimi†, Yutaka Tagaya†, Takeo Sato*, Taeko Yokochi-Fukuda*, Thomas A. Waldmann†, Tadatsugu Taniguchi* & Shinsuke Taki*

* Department of Immunology, Graduate School of Medicine and Faculty of Medicine, University of Tokyo, Hongo 7-3-1, Bunkyo-ku, Tokyo 113, Japan
† Metabolism Branch, National Cancer Institute, National Institutes of Health, Building 10, 9000 Rockville Pike, Bethesda, Maryland 20892, USA

Natural killer (NK) cells are critical for both innate and adaptive immunity[1,2]. The development of NK cells requires interactions between their progenitors and the bone-marrow microenvironment[3–6]; however, little is known about the molecular nature of such interactions. Mice that do not express the transcription factor interferon-regulatory factor-1 (IRF-1; such mice are IRF-$1^{-/-}$ mice) have been shown to exhibit a severe NK-cell deficiency[7,8]. Here we demonstrate that the lack of IRF-1 affects the radiation-resistant cells that constitute the microenvironment required for NK-cell development, but not the NK-cell progenitors themselves. We also show that IRF-$1^{-/-}$ bone-marrow cells can generate functional NK cells when cultured with the cytokine interleukin-15 (refs 9–12) and that the interleukin-15 gene is transcriptionally regulated by IRF-1. These results reveal, for the first time, a molecular mechanism by which the bone-marrow microenvironment supports NK-cell development.

In order to identify which cell population(s) is affected by IRF-1 deficiency, we first transferred bone-marrow cells from IRF-$1^{-/-}$ mice[13] that had been backcrossed several times with C57BL/6 (B6) mice into irradiated, H–2-compatible 129/SvJ (129) mice. In these chimaeric mice, donor-derived lymphoid cells can be distinguished from recipient lymphoid cells by the expression of Ly9.1, a marker protein that is expressed on lymphoid cells in 129 mice but not in B6 mice. As seen in Fig. 1a, irradiated 129 mice into which IRF-$1^{-/-}$ bone-marrow cells had been transferred (IRF-$1^{-/-} \rightarrow$ 129 chimaeras) generated NK cells, which were defined by the expression of NK1.1 and lack of expression of Ly9.1 and CD3 on their surfaces. Similar numbers of NK cells were produced in IRF-$1^{-/-} \rightarrow$ 129 chimaeras and control wild-type B6 $\rightarrow$ 129 chimaeras. Mononuclear cells isolated from mice reconstituted with either IRF-$1^{-/-}$ bone-marrow cells or control wild-type bone-marrow cells exhibited comparable cytotoxicity against NK-sensitive YAC-1 cells (Fig. 1b). Therefore, NK cells generated in IRF-$1^{-/-} \rightarrow$ 129 chimaeras are functional. Complement-dependent elimination of NK cells using a monoclonal antibody against NK1.1 molecules (which is expressed by B6 but not by 129-derived NK cells) abolished cytotoxicity against YAC-1 cells, demonstrating that donor-derived NK cells are responsible for this cytotoxicity (data not shown). Hence, these results demonstrate that bone-marrow cells in IRF-$1^{-/-}$ mice are fully competent to differentiate into functional NK cells if an appropriate environment is provided by normal, radiation-resistant cells.

To confirm this, we transferred bone-marrow cells from 129 mice into irradiated IRF-$1^{-/-}$ mice. In this case NK cells were detected by their expression of Ly9.1 and the interleukin-2 receptor-β (IL-2Rβ) chain, another marker for NK cells[14]. As shown in Fig. 2a, $129 \rightarrow$ IRF-$1^{-/-}$ chimaeras generated significantly fewer NK (Ly9.1$^+$IL-2Rβ$^+$CD3$^-$) cells than did control $129 \rightarrow$ wild-type chi-
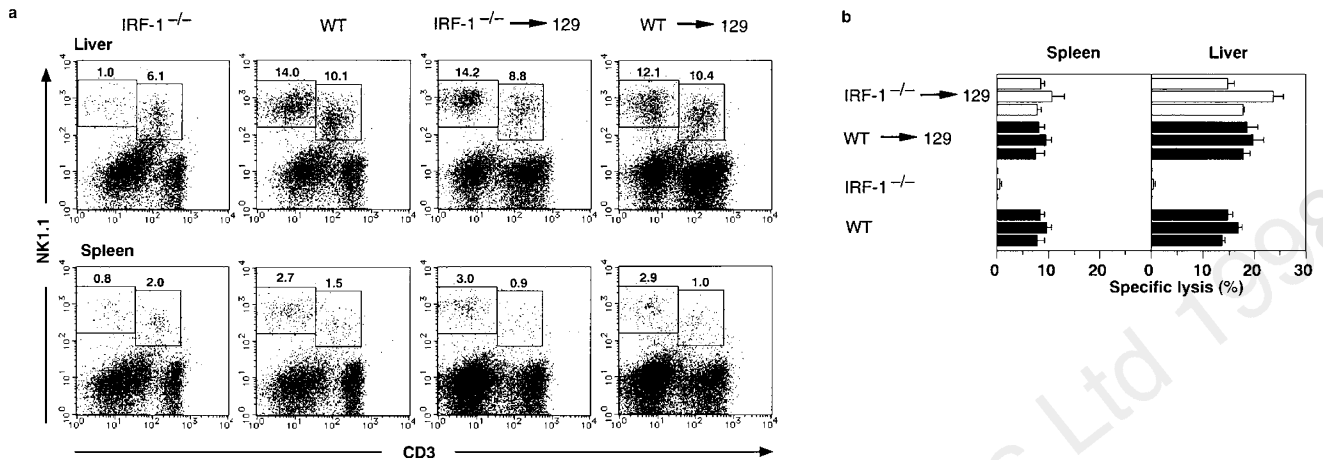
Figure 1 Generation of NK cells from bone-marrow cells upon transfer into irradiated wild-type (WT) mice. **a**, Flow cytometry analysis of the NK (NK1.1+CD3−) or NK-T (NK1.1+CD3+) cell populations in the liver (upper row) or the spleen (lower row) of IRF-1−/− → 129 or WT → 129 chimaeras. Profiles representing unmanipulated IRF-1−/− and wild-type mice are also included as controls. Cells expressing Ly9.1 (<10% in all cases) were excluded from the analysis. The x-axis shows the fluorescent intensity of CD3-staining and the y-axis shows the fluorescent intensity of NK1.1-staining. The numbers in each profile indicate the percentages of cells within indicated quadrants. Representative data from one of three independent transfers are shown. **b**, Natural cytotoxicity (mean % specific lysis and s.e.m. of triplicated assays) of spleen and liver NK cells in indicated chimaeric or unmanipulated mice. Each column represents the result obtained from a single animal assayed at the effector-to-target (E/T) ratio of 50 (liver) or 200 (spleen).

maeras, and functional NK cells were totally absent in both the spleen and the liver of 129 → IRF-1−/− chimaeras (Fig. 2b). We imagine that this partial restoration of the development, but not function, of NK cells may be due to the transfer of some radiation-resistant cells from the donor bone marrow. These results show that IRF-1 is dispensable for the generation of NK-cell progenitors but essential for the function of radiation-resistant cells in supporting NK-cell development. Supporting this notion, we found a similar percentage of CD45 R/B220+CD19−NK1.1+ cells, which may be NK-cell progenitors[15], in the bone marrow of IRF-1−/− and wild-type mice (data not shown).

These observations indicate the existence of an IRF-1 target gene(s) which is required to 'nurture' the development of functional NK cells. Much evidence points to the paramount role of cytokines in lymphopoiesis. In particular, interleukin (IL)-5 (refs 9–12) is seen as a key cytokine in NK-cell development, for several reasons. First, NK-cell development is impaired in mice lacking the IL-2Rβ or IL-2Rγ chains, which are shared by the IL-2 and IL-15 receptors[16–18]. Second, NK cells develop normally in mice lacking IL-2 or the IL-2Rα chain[19]. Third, recombinant IL-15 (rIL-15) induces NK-cell differentiation in human bone-marrow cultures[20].

We therefore examined whether exogenous rIL-15 could restore the ability of IRF-1−/− bone-marrow cells to create an environment that is permissive for NK-cell development. Interestingly, in the presence of rIL-15, as many functional NK cells were generated *in vitro* from IRF-1−/− bone-marrow cells as were produced from wild-type bone-marrow cells (Fig. 3a and b). In contrast, IL-7, which induced B-cell differentiation from wild-type or IRF-1−/− bone-marrow cells (data not shown), did not induce NK-cell differentiation (Fig. 3a and b). As IL-15 can confer cytotoxicity to nonlytic NK cells in β-oestradiol-treated mice[21], it seems to support not only NK-cell development from bone-marrow progenitors, but also the acquisition of cytolytic activity by mature NK cells. However, NK cells generated from IL-15-supplemented IRF-1−/− bone-marrow-cell culture showed significantly less lytic activity than those from wild-type bone-marrow cells (Fig. 3b). This result points to the interesting possibility that IRF-1 controls the expression of an as-yet-unidentified target gene(s) that contributes to the acquisition of cytotoxicity. Nevertheless, these results strongly suggest that the impairment of NK-cell development is due to defects in IL-15 production in IRF-1−/− mice and that the *IL-15* gene is a target of IRF-1.
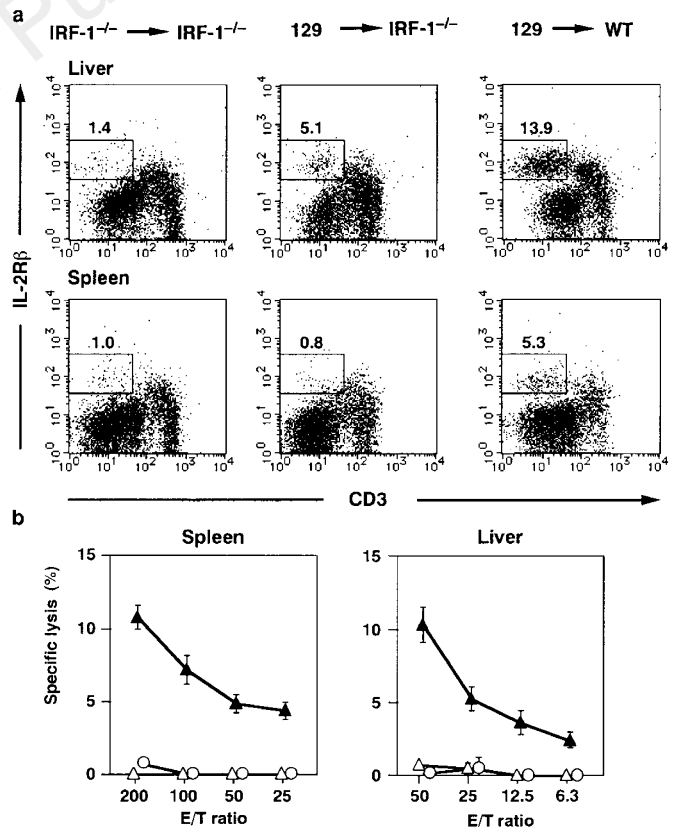

Figure 2 Inability of irradiated IRF-1−/− mice to support NK-cell development from wild-type bone-marrow cells. **a**, Flow cytometry profiles for IRF-1−/− mice which had received either IRF-1−/− (IRF-1−/− → IRF-1−/−) or wild-type (129 → IRF-1−/−) bone-marrow cells. The result obtained from a control transfer (129 → wild-type, WT) is also shown. Donor-derived cells constituted more than 90% of total lymphocytes. The number in each profile indicates the percentage of NK (IL-2Rβ+CD3−) cells. **b**, NK-cell-mediated cytotoxicity of IRF-1−/− → IRF-1−/− (open circles), 129 → IRF-1−/− (open triangles) and 129 → WT (filled triangles) chimaeras. Each symbol represents the mean and the s.e.m. of triplicate assays. Representative data from one of three independent transfers are shown. We infer that the non-lytic NK cells present in 129 → IRF-1−/− chimaeras developed as a result of the partial reconstitution of the environment in the host IRF-1−/− mice by donor bone marrow derived cells. E/T, effector-to-target ratio.

Within the 5′-upstream region of the *IL-15* gene we found a 13-base-pair sequence, TCTTTCACTTTTC, spanning from positions −348 to −336 relative to the cap site (N.A., unpublished observations, and ref. 22). This sequence is the same as the consensus IRF-1-responsive element (IRF-E)[23]. Indeed, we found that this sequence motif binds the IRF-1 protein specifically (data not shown). This IRF-E motif is critical for the activation of the IL-15 promoter, as shown by co-transfection assays in which IL-15-promoter fragments, with or without this motif, were fused to the luciferase-reporter plasmid and co-transfected with an IRF-1-expression vector into P19 cells (Fig. 4a). In addition, a synthetic oligomer representing this motif alone could confer IRF-1-induced responses when ligated to a heterologous promoter in the same co-transfection assay (data not shown).

In wild-type bone-marrow cells, expression of *IL-15* messenger RNA could be strongly induced by combined stimulation with lipopolysaccharide (LPS) and interferon (IFN)-γ *in vitro*[10,24] (Fig. 4b). In contrast, induction of transcription of the *IL-15* gene was barely detectable in IRF-1^{−/−} bone-marrow cells. Thus, IRF-1 indeed controls induction of transcription of the *IL-15* gene. Similar low-level expression of *IL-15* mRNA was observed by reverse transcription with polymerase chain reaction (PCR) analysis in both unstimulated IRF-1^{−/−} and wild-type bone-marrow cells (data not shown), indicating that IRF-1 is responsible for the induction of expression, but not the constitutive expression, of the *IL-15* gene. This observation suggests that, during the natural course of NK-cell

development, there must be some stimulus that induces IL-15 in an IRF-1-dependent manner and which is required for development. IRF-1 is induced by a variety of stimuli, including IFN-γ (ref. 25), although this stimulus is unlikely to be IFN-γ itself as NK-cell development proceeds normally in mice lacking IFN-γ or its receptor[26,27]. The identification of such a stimulatory ligand or factor would be an interesting avenue to follow.

It is interesting that the development of NK1.1^{+}CD3^{+} cells, so-called NK-T cells[28], is not markedly affected in IRF-1^{−/−} mice (Fig. 1a). This finding indicates that the environment required for NK-T-cell development is distinct from that for NK-cell development with respect to the requirement for IRF-1 and IL-15, despite the apparently common origin of these cells[28,29]. Identification of the signals that lead to the expression of IRF-1 and additional target genes, as well as the cell type responsible for the production of IL-15, will help us to dissect the intricate progenitor–environment interactions occurring during the lineage commitment of lymphoid cells. □

Methods

Bone-marrow transplantation and analysis of NK-cell development. IRF-1^{−/−} mice used as both donors and recipients of bone-marrow transplantation had been backcrossed five times with B6 mice. 1×10^7 bone-marrow cells were transferred intravenously into irradiated mice (absorbed dose of radiation: 8.5 gray for 129 and IRF-1^{−/−} mice, and 9.0 gray for wild-type mice). Mononuclear cells isolated from the spleen and liver[8] were analysed 8 to 10 weeks after bone-marrow transfer, by using flow cytometry with a FACScalibur and CellQuest software (Becton) with fluorochrome-conjugated monoclonal antibodies against Ly9.1, NK1.1, CD3 and IL-2Rβ (Pharmingen). To measure NK-mediated cytotoxicity, the standard cytotoxic assay against YAC-1 cells was performed as described previously[8] using several different effector-to-target (E/T) ratios.

In vitro **generation of NK cells.** Bone-marrow cells were cultured in RPMI-
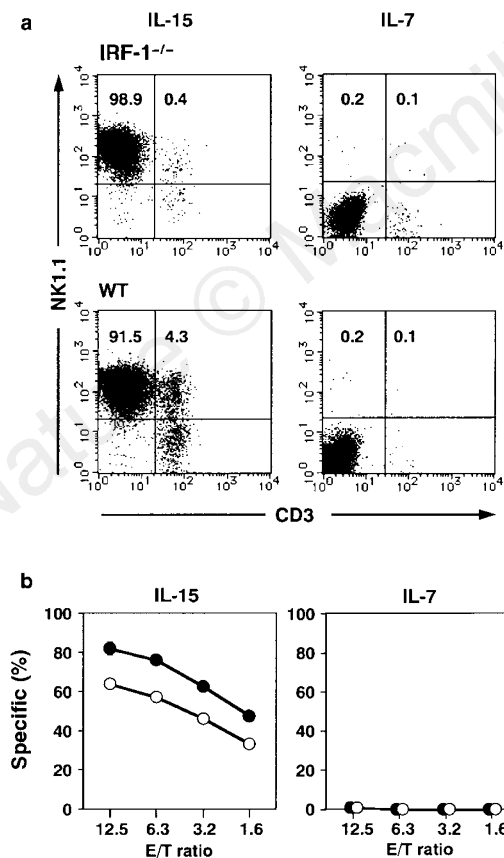

Figure 3 *In vitro* compensation of IRF-1 deficiency by IL-15. **a**, Generation of NK cells (NK1.1^{+}CD3^{−}) from IRF-1^{−/−} (upper row) or wild-type (WT; lower row) bone-marrow cells in culture supplemented with recombinant IL-15 or recombinant IL-7 *in vitro*. Representative data from three independent cultures are shown. **b**, Cytotoxicity of NK cells generated *in vitro* from IRF-1^{−/−} (open circles) or wild-type (filled circles) bone-marrow cells. Data represent the mean of triplicate assays. The s.e.m.s for individual determinations fall within the symbols and therefore cannot be seen. This experiment was repeated three times with similar results. E/T, effector-to-target ratio.
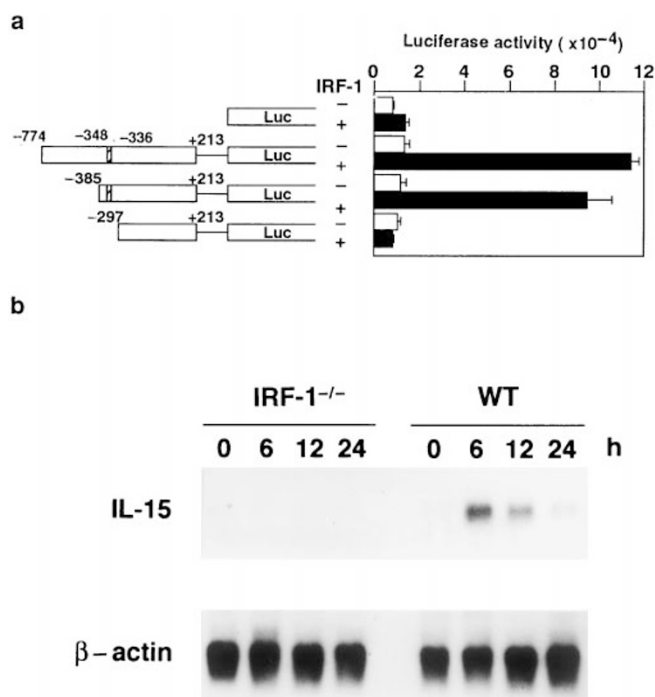

Figure 4 IRF-1 regulates the expression of the *IL-15* gene. **a**, Reporter constructs driven from the *IL-15* promoter containing or lacking the IRF-1-responsive element (cross-hatched area) were transfected together with IRF-1-expression (filled columns) or control (open columns) vectors, and luciferase (Luc) activity was measured. **b**, Expression of *IL-15* mRNA in bone-marrow cells. Total RNA prepared from IRF-1^{−/−} and wild-type (WT) bone-marrow cells which had been stimulated with IFN-γ and LPS for 0, 6, 12 and 24 h were probed for IL-15 and β-actin mRNA expression.

1640 medium containing 10% FCS and either simian rIL-15 (Genzyme, 60 ng ml^{-1}) or murine recombinant IL-7 (R&D, 10 ng ml^{-1}) for 10 days. Cells recovered from cultures were analysed by flow cytometry or in the cytotoxicity assay.

Plasmid construction and luciferase assay. A DNA fragment spanning from positions −774 to +213 of the *IL-15* gene (N.A. and Y.T., unpublished observations) was cloned into a luciferase reporter plasmid (Promega) either directly or after deleting 5′ portions. Synthetic oligomers representing the potential IRF-E in the promoter region of the *IL-15* gene were inserted along with downstream human IFN-β-promoter elements (−55 to +19 region) into the Picagene luciferase reporter plasmid (Wako)[30]. Reporter constructs were then transfected with IRF-1-expression (pAct-1) or control (pAct-C) vectors into P19 cells, which express no endogenous IRF-1, and luciferase activity was measured as previously described[30].

Analysis of *IL-15* gene expression. Bone marrow cells were cultured in the presence of LPS (30 μg ml^{-1}) and IFN-γ (100 units ml^{-1}). Total RNA was isolated by acid guanidium thiocyanate–phenol–chloroform extraction and subjected to northern blot analysis as previously described[30]. Mouse *IL-15* and β-actin complementary DNA probes obtained by PCR were used for hybridization.

Received 16 September; accepted 24 November 1997.

1. Trinchieri, G. Biology of natural killer cells. *Adv. Immunol.* **47**, 187–376 (1989).
2. Scott, P. & Trinchieri, G. The role of natural killer cells in host–parasite interactions. *Curr. Opin. Immunol.* **7**, 34–40 (1995).
3. Haller, O. & Wigzell, H. Suppression of natural killer cell activity with radioactive strontium: effector cells are marrow dependent. *J. Immunol.* **118**, 1503–1506 (1977).
4. Seaman, W. E., Gindhart, T. D., Greenspan, J. S., Blackman, M. A. & Talal, N. Natural killer cells, bone, and the bone marrow: studies in estrogen-treated mice and in congenitally osteopetrotic (mi/mi) mice. *J. Immunol.* **122**, 2541–2547 (1979).
5. Kumar, V., Ben-Ezra, J., Bennett, M. & Sonnenfeld, G. Natural killer cells in mice treated with [89]strontium: normal target-binding cell numbers but inability to kill even after interferon administration. *J. Immunol.* **123**, 1832–1838 (1979).
6. Hackett, J. Jr, Bennett, M. & Kumar, V. Origin and differentiation of natural killer cells. I. Characteristics of a transplantable NK cell precursor. *J. Immunol.* **134**, 3731–3738 (1985).
7. Duncan, G. S., Mittrücker, H.-W., Kägi, D., Matsuyama, T. & Mak, T. W. The transcription factor interferon regulatory factor-1 is essential for natural killer cell function *in vivo*. *J. Exp. Med.* **184**, 2043–2048 (1996).
8. Taki, S. *et al.* Multistage regulation of Th1-type immune responses by the transcription factor IRF-1. *Immunity* **6**, 673–679 (1997).
9. Giri, J. G. *et al.* Utilization of the β and γ chains of the IL-2 receptor by the novel cytokine IL-15. *EMBO J.* **13**, 2822–2830 (1994).
10. Grabstein, K. H. *et al.* Cloning of a T cell growth factor that interacts with the β chain of the interleukin-2 receptor. *Science* **264**, 965–968 (1994).
11. Carson, W. E. *et al.* Interleukin (IL) 15 is a novel cytokine that activates human natural killer cells via components of the IL-2 receptor. *J. Exp. Med.* **180**, 1395–1403 (1994).
12. Tagaya, Y., Bamford, R. N., DeFilippis, A. P. & Waldmann, T. A. IL-15: a pleiotropic cytokine with diverse receptor/signaling pathways whose expression is controlled at multiple levels. *Immunity* **4**, 329–336 (1996).
13. Matsuyama, T. *et al.* Targeted disruption of IRF-1 or IRF-2 results in abnormal type I IFN gene induction and aberrant lymphocyte development. *Cell* **75**, 83–97 (1993).
14. Tanaka, T. *et al.* Selective long-term elimination of natural killer cells *in vivo* by an anti-interleukin 2 receptor β chain monoclonal antibody in mice. *J. Exp. Med.* **178**, 1103–1107 (1993).
15. Rolink, A. *et al.* A subpopulation of B220+ cells in murine bone marrow does not express CD19 and contains natural killer cell progenitors. *J. Exp. Med.* **83**, 187–194 (1996).
16. DiSanto, J. P., Muller, W., Guy-Grand, D., Fischer, A. & Rajewsky, K. Lymphoid development in mice with a targeted deletion of the interleukin 2 receptor γ chain. *Proc. Natl Acad. Sci. USA* **92**, 377–381 (1995).
17. Ohbo, K. *et al.* Modulation of hematopoiesis in mice with a truncated mutant of the interleukin-2 receptor γ chain. *Blood* **87**, 956–967 (1996).
18. Suzuki, H., Duncan, G. S., Takimoto, H. & Mak, T. W. Abnormal development of intestinal intraepithelial lymphocytes and peripheral natural killer cells in mice lacking the IL-2 receptor β chain. *J. Exp. Med.* **185**, 499–505 (1997).
19. DiSanto, J. P. Shared receptors, distinct functions. *Curr. Biol.* **7**, R424–R426 (1997).
20. Mrozek, E., Anderson, P. & Caligiuri, M. A. Role of interleukin-15 in the development of human CD56+ natural killer cells from CD34+ hematopoietic progenitor cells. *Blood* **87**, 2632–2640 (1996).
21. Puzanov, I. J., Bennett, M. & Kumar, V. IL-15 can substitute for the marrow microenvironment in the differentiation of natural killer cells. *J. Immunol.* **157**, 4282–4285 (1996).
22. Anderson, D. M. *et al.* Chromosomal assignment and genomic structure of IL-15. *Genomics* **25**, 701–706 (1995).
23. Tanaka, N., Kawakami, T. & Taniguchi, T. Recognition DNA sequences of interferon regulatory factor 1 (IRF-1) and IRF-2, regulators of cell growth and the interferon system. *Mol. Cell. Biol.* **13**, 4531–4538 (1993).
24. Bamford, R. N., Battiata, A. P., Burton, J. D., Sharma, H. & Waldmann, T. A. Interleukin (IL) 15/IL-T production by the adult T-cell leukemia cell line HuT-102 is associated with a human T-cell lymphotrophic virus type I region/IL-15 fusion message that lacks many upstream AUGs that normally attenuates IL-15 mRNA translation. *Proc. Natl Acad. Sci. USA* **93**, 2897–2902 (1996).
25. Taniguchi, T., Lamphier, M. S. & Tanaka, N. IRF-1: the transcription factor linking the interferon response and oncogenesis. *Biochim. Biophys. Acta* **1333**, M9–M17 (1997).
26. Dalton, D. K. *et al.* Multiple defects of immune cell function in mice with disrupted interferon-γ genes. *Science* **259**, 1739–1742 (1993).
27. Huang, S. *et al.* Immune response in mice that lack the interferon-γ receptor. *Science* **259**, 1742–1745 (1993).
28. Bendelac, A., Rivera, M. N., Park, S. H. & Roark, J. H. Mouse CD1-specific NK1 T cells: development, specificity, and function. *Annu. Rev. Immunol.* **15**, 535–562 (1997).
29. Rodewald, H. R. *et al.* A population of early fetal thymocytes expressing FcγRII/III contains precursors of T lymphocytes and natural killer cells. *Cell* **69**, 139–150 (1992).
30. Tan, R. S., Taniguchi, T. & Harada, H. Identification of the lysyl oxidase gene as target of the antioncogenic transcription factor, IRF-1, and its possible role in tumor supression. *Cancer Res.* **56**, 2417–2421 (1996).

Immunoreceptor DAP12 bearing a tyrosine-based activation motif is involved in activating NK cells

Lewis L. Lanier, Brian C. Corliss, Jun Wu, Clement Leong & Joseph H. Phillips

DNAX Research Institute of Molecular and Cellular Biology, Department of Immunobiology, 901 California Avenue, Palo Alto, California 94304, USA

Natural killer (NK) cells express cell-surface receptors of the immunoglobulin and C-type lectin superfamilies that recognize major histocompatibility complex (MHC) class I peptides and inhibit NK-cell-mediated cytotoxicity[1]. These inhibitory receptors possess ITIM sequences (for immunoreceptor tyrosine-based inhibitory motifs) in their cytoplasmic domains that recruit SH2-domain-containing protein tyrosine phosphatases, resulting in inactivation of NK cells[2–4]. Certain isoforms of these NK-cell receptors lack ITIM sequences and it has been proposed that these 'non-inhibitory' receptors may activate, rather than inhibit, NK cells[4–6]. Here we show that DAP12, a disulphide-bonded homodimer containing an immunoreceptor tyrosine-based activation motif (ITAM) in its cytoplasmic domain, non-covalently associates with membrane glycoproteins of the killer-cell inhibitory receptor (KIR) family without an ITIM in their cytoplasmic domain. Crosslinking of KIR–DAP12 complexes results in cellular activation, as demonstrated by tyrosine phosphorylation of cellular proteins and upregulation of early-activation antigens. Phosphorylated DAP12 peptides bind ZAP-70 and Syk protein tyrosine kinases, suggesting that the activation pathway is similar to that of the T- and B-cell antigen receptors.

It has been reported that an unknown phosphoprotein of relative molecular mass (M_r) ∼12,000, expressed as a disulphide-bonded dimer, was coimmunoprecipitated from NK-cell lysates together with a non-inhibitory KIR2DS2 glycoprotein (a KIR family member with two immunoglobulin-domains in the extracellular domain, a short cytoplasmic domain lacking an ITIM, and a charged residue in the transmembrane region that is a receptor for HLA-C ligands, also referred to as p50.2 or KAR)[7]. Cell-surface immunoglobulin receptors, T-cell antigen receptors (TCR), and certain Fc receptors (FcR) non-covalently associate with small transmembrane proteins (such as CD3δ,γ,ε,ζ subunits, CD79α,β, FcεRI-γ) containing ITAM sequences (D/ExxYxxL/I − x$_{6–8}$ − YxxL/I)[8] that are required for signal transduction by these receptor complexes[9]. Therefore, it seems likely that these non-inhibitory NK-cell receptors might require an associated protein with similar properties to mediate positive signal transduction.

A database of expressed tag sequences (EST) from a large panel of complementary DNA libraries was searched with a TBLASTN algorithm program for molecules bearing homology with the human CD3δ,γ,ε,ζ and FcεRI-γ protein sequences. An EST from a human CD1+ dendritic cell library was selected for further study